VORTEX-INDUCED VIBRATIONS OF AN ELASTIC CIRCULAR CYLINDER

C. Y. Zhou, R. M. C. So and K. Lam

*Department of Mechanical Engineering, The Hong Kong Polytechnic University,
Hung Hom, Kowloon, Hong Kong*

A numerical study of a uniform flow past an elastic circular cylinder using the discrete vortex method incorporating the vortex-in-cell (VIC) technique has been undertaken. The Reynolds number is kept at 200 for all calculations and the cylinder motion is modelled by a spring–damper–mass system. The fluid motion and the structural responses are solved in an iterative way so that the interactions between the fluid and the structure can be accounted for properly. Analyses of the cylinder responses, the damping, the induced forces, the vortex shedding frequency and the vortex structure in the wake have been carried out. The results show that fluid damping is responsible for a limit-cycle oscillation behaviour even when the system natural frequency is close to the vortex-shedding frequency. Reasonable agreement with previous experimental data and computational results is obtained in the comparison of the amplitude of the limit-cycle oscillations. The results further show that the cylinder oscillations could be as large as 0·57 diameter under certain flow conditions and structural properties. Finally, it is shown that a one-degree-of-freedom structural model yields results that are only in qualitative agreement with a two-degree-of-freedom model. In other words, the streamwise oscillations also have a substantial effect on the transverse vibrations and their characteristics.

© 1999 Academic Press

1. INTRODUCTION

FLUID-STRUCTURE INTERACTIONS occur in many engineering fields. These interactions give rise to complicated vibrations of the structures and could cause structural damage under certain unfavourable conditions. A common fluid-structure interaction problem is the flow-induced vibrations on a structure caused by vortex shedding from the structure. Numerous experimental and numerical studies have been carried out on this fluid-structure interaction problem. Early experimental studies concentrated on rigid structures in a cross-flow (Richter & Naudascher 1976; So & Savkar 1981; Baban *et al.* 1989). Later investigations dealt with elastic structures because of their importance in many engineering fields (Feireisen *et al.* 1994; West & Apelt 1997). In spite of these later studies, the investigations of fluid-structure interactions as a fully coupled problem are far from complete.

Different experimental approaches could be used to investigate flow-induced vibrations, depending on the kind of data that the studies set out to obtain. For example, if the effects of the structural vibrations on the wake behaviour are of interest only, the approach adopted is to force the structure to vibrate (usually in one direction) at prescribed amplitude and frequency. Numerous experimental studies have been carried out on a forced oscillating structure; some representative investigations are those of Koopman (1967), Griffin & Votaw (1972), and Griffin & Ramberg (1974). The vibrations alter the vortex pattern and change the spacing between vortices in the wake. In this type of experiment, not all of the data

obtained represent the characteristics of a fully coupled flow-induced vibration problem (Parkinson 1989) because the experiments are not designed to examine the feedback from the flow.

An alternative is to experimentally simulate flow-induced vibrations directly; thus ensuring that the data obtained can shed light on the nonlinear interactions between excitation and response that are central to the fluid-structure interaction problem. Representative studies carried out on elastic circular cylinders are the experiments of Feng (1968), Griffin & Koopmann (1977), Griffin (1980) and Griffin & Ramberg (1982). These studies, which covered a range of Reynolds number (Re), show that the vortex-induced vibration is a self-limiting process. The cross-flow vibration amplitude has a strong relationship with the phase difference between the lift force and the cylinder motion. Furthermore, the vibration amplitude depends on a reduced damping parameter, $Sg = 8\pi^2 St^2 \alpha M^*$, which was derived by Griffin (1992) after analysing a group of data collected from different experiments. Here, $St = f_s D/U_\infty$ is the Strouhal number, $M^* = m/\rho D^2$ is the mass ratio, α is the damping factor in the structural dynamic equations, D is the cylinder diameter, U_∞ is the undisturbed freestream velocity, f_s is the vortex shedding frequency, m is the mass per unit length of the cylinder and ρ is the fluid density. When the mass ratio is small, the effective mass which includes the cylinder mass plus the added mass is important as it influences the characteristics of the fluid-structure system, such as the natural frequency and the damping ratio. Recently, Khalak & Williamson (1996) examined a hydroelastic cylinder with a very low mass damping in a cross-flow. Their results show that the response of the cylinder has two resonance branches, a lower branch and an upper branch, with a discontinuous transition between the two. This behaviour has also been found by Brika & Laneville (1993), who conducted a similar experiment in air for a relatively high mass ratio. Fairly comprehensive reviews on this fluid-structure interaction problem can be found in the articles by Sarpkaya (1979), Bearman (1984) and Parkinson (1989).

On the other hand, much less numerical work has been carried out, because of the numerical complexity associated with the problem. Conventional approaches usually decoupled the flow solution from the structural problem. A typical example can be found in the study of aeroelasticity and flutter (Hall 1994). This approach cannot be used to study the interactions between the fluid and the structure. These interactions often play an important role in determining the behaviour of the structure and the development of the flow in the wake. Various numerical approaches have been proposed in the past to treat the fully coupled problem. A recent proposal is a time-marching technique that iterates for the interaction effects at every time step (Jadic *et al.* 1998; So *et al.* 1998). The technique was applied to treat the problem of an elastic airfoil in a uniform flow with discrete vortices in the free-stream over a range of Re. The interactions between the fluid and the structure were considered by solving the equations governing the flow field and the structural motions in an iterative way. The flow equations were solved by the boundary element method, while the vorticity transport equations were resolved by using the operator-splitting technique. A two-degree-of-freedom model was used to approximate the structural dynamic behaviour. Their results showed good agreement with previous flutter calculations in the prediction of the natural frequencies, damping ratios and flutter speed. Furthermore, they have been able to identify the source of nonlinearity, which derives mainly from the moving boundary conditions of the airfoil. In their problem, there was no flow separation; therefore, their technique needs modification before it can be used to calculate the flow around bluff bodies. Newman & Karniadakis (1997) carried out a direct numerical simulation study of the flow past an elastic cable using body-fitted coordinates. Their simulations were carried out for two-dimensional as well as three-dimensional flows at a fairly low Re. The three-dimensional simulations showed a greater Re dependence than the two-dimensional

simulations. Their study focused both on the flow and the hydrodynamic loads induced on the structure and is one of the first studies that deal with the fully coupled problem of flow-induced vibrations on bluff bodies.

Among the different numerical methods in fluid mechanics, the discrete vortex method plays an important role in the study of flow around bluff bodies since it has the advantage of concentrating on the vortical region and capturing the dominant features of vortex shedding from the bluff bodies. The method represents the flow field by a sequence of discrete vortices and solves it by tracking the evolution of the vortices. The method is only suitable for incompressible flows and is naturally grid independent since it uses the Biot–Savart law to calculate the velocity of each vortex. It was originally proposed for inviscid flows and further extended for viscous flows with the incorporations of the random walk technique (Chorin 1973; Stansby & Smith 1983) and a finite-difference scheme (Graham 1988). Since a large number of vortices are needed to represent the flow field (typically 10^4–10^5), using the Biot–Savart law to determine the velocity field becomes too expensive in terms of CPU time. As a result, the vortex-in-cell (VIC) method has been introduced (Christiansen 1973). The key of the development is to by-pass the Biot–Savart law and to project the vorticity from the vortices onto a fixed mesh, so that the velocity field can be calculated through the use of the Poisson equation for the stream function. The VIC discrete vortex method provides substantial savings to the computational time required. However, it makes the method grid-dependent. There are other methods to speed up the Biot–Savart vortex–vortex interaction calculations, e.g. the multiple expansion method of Carrier et $al.$ (1988). So far, for the two-dimensional viscous flow around a rigid structure, the VIC discrete vortex method has been very successful in predicting the force, the vortex pattern and the vortex-shedding frequency (Stansby & Smith 1991; Graham et $al.$ 1993; Meneghini & Bearman 1993; Zhou 1994; Downie et $al.$ 1995). The method has also been extended to treat the flow around two cylinders in tandem and in a side-by-side arrangement (Slaouti & Stansby 1992).

Much less work has been carried out on an elastic structure using the VIC discrete vortex method though. Recently, Slaouti & Stansby (1994) carried out an analysis of the forced and free vibration of a flexible circular cylinder in a current using the VIC random walk vortex method. A two-degree-of-freedom model is assumed for the translational motions of the cylinder. Their investigations were carried out for a range of reduced velocity but for a fixed value of Sg and M^*. For the free vibration case, only the time history results of the lift and drag coefficient and the corresponding displacements along these directions are presented. A discussion on the locking-on phenomenon was given; however, an in-depth analysis of the fluid–structure interactions was not presented. Consequently, an understanding of the fluid–structure interactions of this simple problem is still lacking.

The present study proposes to examine in detail the fluid–structure interaction of a two-dimensional flow past an elastic circular cylinder using the VIC discrete vortex method (Graham 1988), where a finite-difference scheme is adopted to solve for vorticity diffusion. The motion of the structure is modelled by a spring–damper–mass system that only allows translational motion in two directions (a two-degree-of-freedom system). The fluid motion and the cylinder response are solved in an iterative way, so that the interaction between the fluid and the structure can be accounted for propery. The aim of the present work is to examine the vortex-induced vibrations on a circular cylinder and the associated phenomena, such as the response of the cylinder, the unsteady lift and drag on the cylinder, the vortex shedding frequency, and the effects of the cylinder motion on the vortex structure in the wake. As such, it complements the study of Slaouti & Stansby (1994) and devotes considerable attention to examine the interaction behaviour.

In order to establish a baseline for comparison, the flow around a rigid circular cylinder is calculated first. Subsequent calculations are carried out for an elastic circular cylinder with one degree of freedom, where the cylinder is allowed to vibrate only in the transverse direction, and with a two-degree-of-freedom system, where the cylinder is free to respond in both the transverse and streamwise directions. According to Williamson (1991), the upper limit of Re, where the vortex shedding from a circular cylinder is still two-dimensional and the wake is laminar, can reach 200 under carefully controlled experimental conditions. Therefore, Re = 200 is chosen in the present investigation for all calculations.

2. NUMERICAL FORMULATION

2.1. THE VIC DISCRETE VORTEX METHOD

It is assumed that the flow is two-dimensional. For an incompressible viscous fluid, the flow field can be described by the vorticity (ω) transport equation and the Poisson equation for the stream function (ψ),

$$\frac{D\omega}{Dt} = v\nabla^2\omega, \tag{1}$$

$$\nabla^2\psi = -\omega, \tag{2}$$

where v and t are the fluid kinematic viscosity and time, respectively. The fluid at infinity is assumed to be uniform with a velocity U_∞ in the x-direction. The flow starts impulsively. Far downstream, the vorticity is set to zero. On the surface of the cylinder, the nonslip condition is invoked.

A reference frame fixed with the circular cylinder is adopted. In the physical plane $z(x, y)$, a polar mesh is used. The mesh is uniformly spaced in the circumferential direction and exponentially expanded in the radial direction because very fine mesh grids are needed near the surface of the cylinder to resolve the boundary layer. The physical plane is mapped into a computational plane $\zeta(\xi, \eta)$ through a conformal transformation $z = Re^{-i\beta\zeta}$, where R is the radius of the circular cylinder, $\beta = 2\pi/l$ and l is the length of the computational domain in the ξ direction. Thus transformed, the polar mesh in the physical plane is changed to a rectangular mesh in the computational plane as shown in Figure 1(a).

After the transformation, equations (1) and (2) become

$$J\frac{\partial\omega}{\partial t} + \frac{\partial\psi}{\partial\eta}\frac{\partial\omega}{\partial\xi} - \frac{\partial\psi}{\partial\xi}\frac{\partial\omega}{\partial\eta} = v\left(\frac{\partial^2\omega}{\partial\xi^2} + \frac{\partial^2\omega}{\partial\eta^2}\right), \tag{3}$$

$$\frac{\partial^2\psi}{\partial\xi^2} + \frac{\partial^2\psi}{\partial\eta^2} = -J\omega, \tag{4}$$

where J is the Jacobian of the transformation.

In the discrete vortex method, the two-dimensional flow field is represented by a number of point vortices. The vorticity equation (3) is solved by splitting it into two parts (Chorin 1973): a convection part (5) and a diffusion part (6),

$$J\frac{\partial\omega}{\partial t} = -\frac{\partial\psi}{\partial\eta}\frac{\partial\omega}{\partial\xi} + \frac{\partial\psi}{\partial\xi}\frac{\partial\omega}{\partial\eta}, \tag{5}$$

$$J\frac{\partial\omega}{\partial t} = v\left(\frac{\partial^2\omega}{\partial\xi^2} + \frac{\partial^2\omega}{\partial\eta^2}\right). \tag{6}$$

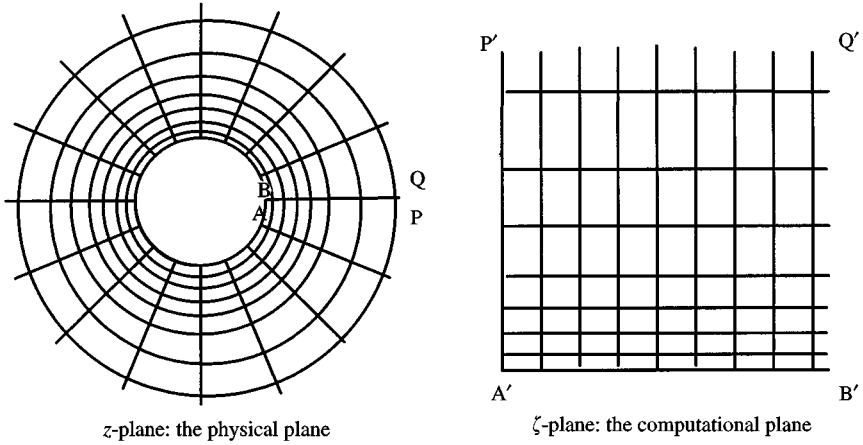z-plane: the physical plane   ζ-plane: the computational plane

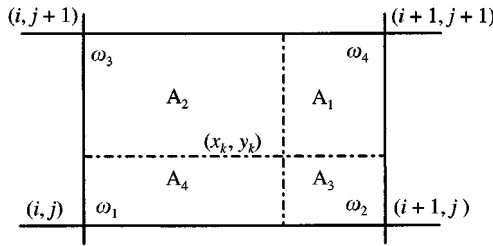Figure 1(a). The meshes in both physical and computational planes.

Figure 1(b). The area-weighting distribution scheme.

The two parts are solved sequentially. Equation (5) is solved by convecting the discrete vortices. The velocity field for convection is obtained by solving the Poisson equation (4) on a mesh where an area-weighting distribution scheme [Figure 1(b)] is used to determine the vorticity on the mesh from the vorticity carried by the point vortices, such that

$$\omega_m = \frac{\Gamma_k A_m}{A^2}, \qquad m = 1, 2, 3, 4.$$

Here, A is the area of the mesh cell and Γ_k is the circulation of the kth vortex. The subscripts indicate the corresponding area or point. Equation (4) is solved on the mesh using the fast Fourier transform with the boundary conditions that on the cylinder surface $\psi = 0$ and at the outer boundary ψ is determined by the Biot–Savart integration. In order to have a more efficient procedure in terms of computational time, the vorticity values at the mesh points rather than the circulation of each discrete vortex are used for the integration [Figure 1(b)]. The contribution of the free-stream is considered separately. The velocity field (u, v) on the mesh is then deduced from the relations $u = \partial\psi/\partial y$ and $v = -\partial\psi/\partial x$, while the velocity of each point vortex is calculated from the velocity values on the mesh, using the following interpolating scheme:

$$u_k = \frac{u_m A_m}{A}, \quad v_k = \frac{v_m A_m}{A}, \qquad m = 1, 2, 3, 4.$$

The vortex particles at (x_k^n, y_k^n) are convected to a new position (x_k^{n+1}, y_k^{n+1}) by the velocity (u_k^n, v_k^n), so that

$$x_k^{n+1} = x_k^n + u_k\Delta t, \quad \text{and} \quad y_k^{n+1} = y_k^n + v_k\Delta t,$$

Since the vorticity has been distributed onto the mesh, the diffusion equation (6) can be solved on the mesh using a finite difference method. For the vorticity boundary conditions, $\omega = 0$ is used at the outer boundary and, on the surface of the body, the vorticity is calculated from the values of ψ and ω at the inner mesh point in such a way that the no-slip boundary condition is satisfied. The change in ω at each grid point due to diffusion is projected back onto the point vortices in the cells around the grid using a similar area-weighting interpolation scheme. With this diffused vorticity field, equation (4) is solved again to give the new velocity field. The point vortices are then convected to new positions. A new vorticity field is obtained by allocating the vorticity from the point vortices onto the mesh through the distribution scheme. This procedure is repeated as many times as required. This two-dimensional hybrid numerical approach was originally based on the work of Graham (1988) and later used/modified by Arkell et al. (1992), Graham et al. (1993), Meneghini & Bearman (1993), and Zhou (1994). It is extended to treat an elastic cylinder in a cross-flow in the present work.

2.2. CYLINDER RESPONSES

It is assumed that the circular cylinder is mounted as a spring–damper–mass system, which represents the situation at a section of a long cylindrical structure at the location of maximum amplitude of vibration. Thus, the motion of the cylinder can be described by the equation

$$\frac{d^2\boldsymbol{\chi}}{dt^2} + 2\alpha\omega_n\frac{d\boldsymbol{\chi}}{dt} + \omega_n^2\boldsymbol{\chi} = \frac{\mathbf{F}(t)}{m}, \tag{7}$$

where $\boldsymbol{\chi} = X\mathbf{i} + Y\mathbf{j}$, X and Y are the instantaneous displacement of the cylinder in the x- and y-directions, respectively; α is the damping factor denoting the damping due to structural dissipation, $\omega_n = \sqrt{k/m} = 2\pi f_n$ is the angular natural frequency of the cylinder, k is the rigidity of the cylinder, and $\mathbf{F}(t)$ is the induced force. Using the cylinder diameter D and the approach velocity U_∞ as the characteristic length and velocity scales, the vibration equation can be written in the dimensionless form

$$\frac{d^2\bar{\Psi}}{d\tau^2} + 4\alpha\pi St^* \frac{f_n}{f_s^*}\frac{d\bar{\Psi}}{d\tau} + \left(2\pi St^* \frac{f_n}{f_s^*}\right)^2 \bar{\Psi} = \frac{\bar{C}_f}{2M^*}, \tag{8}$$

where $\bar{\Psi} = \bar{\chi}/D$ and $\tau = tU_\infty/D$, f_n is the natural frequency of the cylinder, f_s^* is the vortex-shedding frequency of the rigid cylinder, St^* is the Strouhal number for the rigid cylinder defined by $St^* = f_s^*D/U_\infty$ and $\mathbf{C}_f = 2\mathbf{F}(t)/\rho DU_\infty^2$ is the force coefficient. Equation (8) indicates that the response of the cylinder is a function of the damping factor α, the frequency ratio f_n/f_s^*, the mass ratio M^* and also the force coefficient $\mathbf{C}_f$. It is reasonable to assume that the force term on the right-hand side of the equation is a constant within a time step as long as the time step is small enough. The equation can be solved easily using the Runge–Kutta method, once the force coefficient is known from the flow field calculation.

2.3. FORCE CALCULATIONS

The force on the cylinder is calculated by integrating the pressure, p, and the wall shear stress, τ_w, around the cylinder surface. The pressure gradient at the surface can be expressed

as $(\partial p/\partial s)_w = -\nu(\partial \omega/\partial r)_w$ and the wall shear stress is given by $\tau_w = -\mu(\omega)_w$, where μ is the fluid dynamic viscosity. Therefore, the total force is given by

$$F = F_x + iF_y = -\sum_{m=1}^{N} [p_m - i\mu(\omega_m)_w]e^{i\theta m}\Delta s, \qquad (9)$$

where i denotes the unit complex number, s is the curvilinear coordinate along the surface and θ is the corresponding angular coordinate. Normally, the calculated force is noisy since the calculation uses the vorticity gradient. It has been found that the force results are sensitive to the mesh size near the wall, since the calculation depends on the accuracy of the vorticity values stored in the first and second rows of the mesh, and converged as the mesh size becomes finer (Zhou 1994). Therefore, tests were carried out to determine the mesh size and time step for optimum (converged) force results, before the calculations for the present study were conducted. The drag and lift coefficients are given by

$$C_d = \frac{2F_x}{\rho DU_\infty^2} \quad \text{and} \quad C_l = \frac{2F_y}{\rho DU_\infty^2}. \qquad (10a, b)$$

2.4. FLUID-STRUCTURE COUPLING

A reference frame fixed with the cylinder is used. The response of the cylinder is obtained by taking the force of the fluid on the cylinder as the input for the right-hand side of equation (7) and solving equation (7) using the Runge–Kutta method. A flow equal and opposite to that of the cylinder response is superimposed to the flow field due to the reference frame fixed with the cylinder. The flow is then solved subject to this additional velocity. Consequently, an additional term needs to be added to the force coefficient related to the acceleration of the cylinder:

$$C_d^* = C_d + \frac{\pi D}{2U_\infty^2} a_x, \quad C_l^* = C_l + \frac{\pi D}{2U_\infty^2} a_y, \qquad (11a, b)$$

where a_x and a_y are the accelerations of the cylinder in the x and y direction, respectively.

The fluid motion and the cylinder response are solved in an iterative way. In summary, at each time step, the fluid flow is solved using the VIC vortex method. The force on the cylinder is calculated by integrating the pressure and the wall shear stress on the surface. This is then taken as the force input for equation (7) and the response of the cylinder is calculated by solving equation (7) using the Runge–Kutta method. A flow equal and opposite to that of the cylinder response is superimposed to the flow field, because of the use of a reference frame fixed on the cylinder. The fluid motion is solved under this influence in the next time step. Finally, the whole process is repeated in an iterative way so that the interactions between the fluid and the cylinder are accounted for properly.

2.5. COMPUTATIONAL REQUIREMENTS

A typical mesh size used for the calculations is $158 \times 128(r \times \theta)$ covering about $125D$ circular region around the cylinder. The value of the time step Δt is selected to be small enough to satisfy the stability conditions $\nu\Delta t/\Delta\xi^2 < \frac{1}{2}$ and $\nu\Delta t/\Delta\eta^2 < \frac{1}{2}$ because a finite-difference method is used to solve for the diffusion of vorticity. The nondimensional time step, $\Delta t = 0.0025$, is chosen for most of the cases studied under the above considerations. The number of point vortices used is around 10^4–10^5. All the calculations were carried out in a Sun/Ultra 2 workstation. A typical calculation (40 000 time steps) takes about 8 min of CPU time in the Sun/Ultra 2 workstation.

3. DATA ANALYSIS

The present calculations yield time series for the forces, the displacements and the velocity field. Calculations of the statistics, such as mean and root-mean-square values, are quite straightforward. However, evaluations of the frequency characteristics of the time series need some careful consideration. A number of methods are available for the determination of the frequency characteristics of a time series. Among the most commonly used methods is the fast Fourier transform (FFT). The FFT technique works best when the time interval Δt is equal (Bendat & Piersol 1971). Therefore, a time series with N samples at Δt apart will yield N frequency estimates in the domain $[-1/2\Delta t, 1/2\Delta t]$. The frequency resolution is $1/N\Delta t$ (Hz). This frequency resolution may not be fine enough for some situations, especially when the damping of the fluid-structure system is small, where the frequency transfer function demonstrates sharp peaks around the natural frequencies and the vortex-shedding frequency. This drawback could be remedied by increasing the number of samples, i.e., increasing the frequency resolution. This is not always possible because a larger N would lead to an increase in the sampling time, a corresponding increase in the CPU time and a much larger memory. Besides, numerical stability also dictates the minimum Δt that can be used. In view of these limitations, it appears that FFT might not be a suitable data analysis technique for the present problem.

An alternative approach is to adopt the autoregressive moving-averaging (ARMA) identification technique (Mignolet & Red-House 1994). This approach relies on the evaluation of the likelihood function corresponding to measured or calculated (in a numerical simulation experiment) time-series data. There are several steps in this multistage approach. First, it represents the time-series data using an autoregressive (AR) model, which predicts the present values as a linear combination of the past values and a white noise deviate. The model is obtained by solving a linear system of equations. These results are then used to initialize an MA (moving-averaging) matrix polynomial. Afterwards, an iterative procedure is employed to determine the ARMA model that provides, at the same time, a "best" fit of both the time-series data and the AR model. Finally, the estimates of the natural frequencies, damping ratios and mode shapes are obtained from the autoregressive part of the ARMA model. A more detailed discussion of this technique can be found in Mignolet *et al.* (1993) and Mignolet & Red-Horse (1994).

In general, the higher the order of the model, the better the fit between the model and the original time series. However, there are high computational costs associated with an over-determined set of equations and higher-order models. As to the question of how to choose an optimal order for the model, there are various methods (Mignolet *et al.* 1993). In the present investigation, the determination of an appropriate value for the AR order for some cases were performed by examining the effects of the values of the Akaike information criterion (AIC) and the minimum description length (MDL) on the accuracy of the results (Mignolet *et al.* 1993). Theoretically, the optimal order of the AR model is the one when the AIC and MDL have their minima. It is found that the AIC displays several local minima. According to Mignolet & Red-Horse (1994), the AR order, in which the AIC shows a local minimum larger than the value that yields the lowest MDL, is selected.

This ARMA approach gives much better frequency resolution than the FFT method and could be used to identify the frequency characteristics of an elastic structure in a cross-flow. Futhermore, the ARMA technique has also been shown by Jadic *et al.* (1998) and So *et al.* (1998) to give correct results on the damping ratios and mode shapes of an elastic airfoil in a flow with discrete vortices. Damping ratio and mode shape are crucial parameters for the understanding of vibrations. Therefore, it is important to be able to analyse the signals for these properties. This is another advantage of the ARMA technique over that of the FFT

because the latter cannot be used with confidence to deduce information on the damping ratio and mode shape.

In this paper, ARMA is used to analyse all time series thus calculated and the discussion is only concentrated on the frequency content, the wake structure and the effect of the reduced damping parameter. Damping ratios of the flow-induced vibrations will be the subject of a subsequent paper, where the use of ARMA to analyse flow-induced vibration signals compared to other techniques will be discussed in more detail.

4. RIGID CYLINDER WITH Re = 200

In order to establish a baseline for comparison, a uniform flow past a rigid circular cylinder at Re = 200 is calculated first. Figure 2 shows the time histories of the lift and drag coefficients, while Figures 3 and 4 show the vortex pattern and the spectral analysis results of the lift and drag time histories using ARMA, respectively. It can be seen that the lift force settles to a regular sinusoidal function after the onset of wake instability leads to vortex shedding (Figure 2). Similarly, the drag force also settles to a periodic behaviour with a mean value around 1·32. The vortex pattern in the wake shown in Figure 3 composes of negative and positive staggered vortices, i.e. the well-known Karman vortex street. In Figure 4, St* is found to be 0·1922 and the dimensionless frequency of the drag force is determined to be 0·3853, which is about twice that of St*, as expected. In other words, all the salient features of a rigid cylinder in a cross-flow are recovered correctly by the present method.
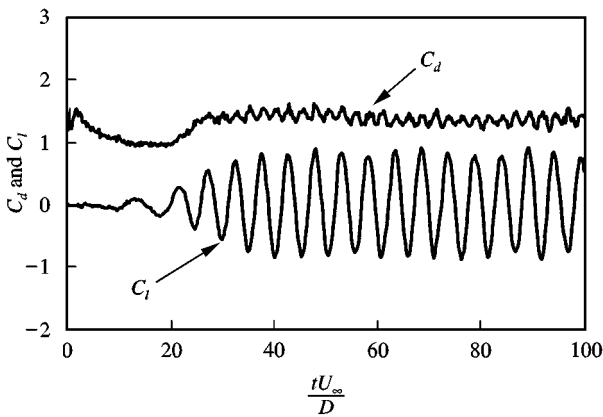

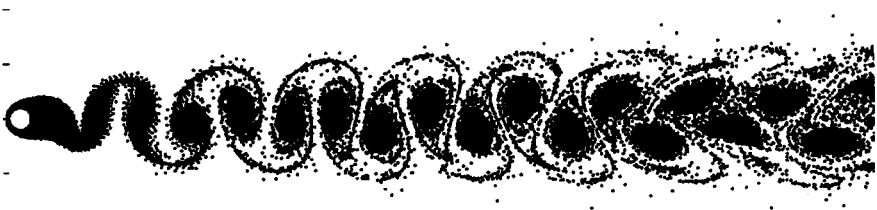Figure 2. Force time histories for a rigid cylinder, Re = 200.

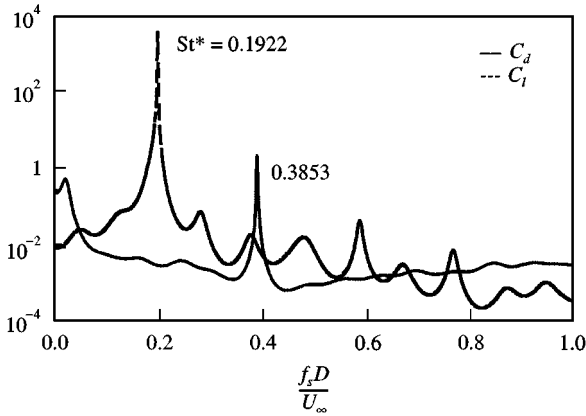Figure 3. The vortex pattern in the wake of a rigid cylinder, Re = 200.

Figure 4. Spectral analysis of the forces for a rigid cylinder, Re = 200.

TABLE 1
Force coefficients and Strouhal number for a rigid cylinder, Re = 100

Investigators	St*	$C_{d\,\text{mean}}$	$C_{l\,\text{rms}}$
Stansby & Slaouti (1993)	0·166	1·317	0·248
Williamson (1989)	0·164	—	—
Present results	0·1620	1·4757	0·2190

A uniform flow with Re = 100 is also calculated to assess the performance of the method. The results are compared with the experimental data of Williamson (1989) and the numerical data of Stansby & Slouti (1993). Only the results obtained by using the polar mesh (Stansby & Slaouti 1993) are chosen for comparison. The results are tabulated in Table 1, and show that the present $C_{d\,\text{mean}}$ is slightly higher while $C_{l\,\text{rms}}$ is lower than those calculated by Stansby & Slaouti (1993) using the random-vortex method. The agreement between the experimentally measured St* and the computational result is quite good though.

5. ELASTIC CYLINDER WITH Re = 200

Calculations were then carried out for an elastic circular cylinder with two degrees of translational freedom for a number of cases where Re = 200 and M^* is chosen as 1 and 10. These parameters were chosen because some experimental and computational data are available for comparison. The reduced damping, Sg, varies from 0·01 to 10 and the frequency ratio, f_n/f_s^*, ranges from 0·65 to 5·2.

Self-limiting process. One of the most important findings in the flow-induced vibrations of a structure is that the vortex-induced vibration is a self-limiting process. Griffin (1992) has compiled numerous experimental data from different investigations and has shown that the amplitude of the vibrations could be correlated by Sg. All the data examined by Griffin (1992) follow a universal curve when plotted against Sg. The behaviour of the curve
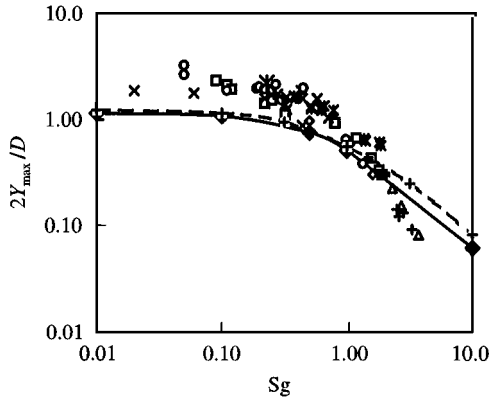
Figure 5. Flow-induced cross-flow vibration amplitude versus Sg. Symbols: experimental data compiled by Griffin (1992); dashed line: calculated results (2-D) of Newmann & Karniadakis (1995) for Re = 200 and $M^* = 1$; solid line: present results for Re = 200 and $M^* = 1$.

is such that the amplitude decreases as Sg increases and approaches a finite limit as Sg decreases.

The nondimensionalized peak-to-peak vibration amplitude, $2Y_{max}/D$, of the present results are plotted versus Sg in Figure 5, together with the data compiled by Griffin (1992) and the two-dimensional computational results of Newman & Karniadakis (1995). It can be seen that the present results show a trend similar to the experimental data and are in good agreement with the computational results of Newman & Karniadakis (1995). Both simulation results show an amplitude-limiting response as Sg approaches zero and a decrease in amplitude as Sg increases. However, for low values of Sg, the simulation results are lower than the experimental data and, for high values of Sg, the opposite trend is observed. The noted discrepancy at high and low values of Sg could be due to Re effects, because Re for the experiments varies from 300 to 10^6, while it is only 200 for the numerical simulations. An alternative reason could be the difference in values of other parameters such as the mass ratio. Another reason for the discrepancy noted in high values of Sg could be attributed to three-dimensionality in the wake. It has been known that structural vibrations normally enhance the spanwise correlation of the wake, i.e. they promote two dimensionality in the wake (Blevins 1994). However, two-dimensional simulation assumes that the spanwise coherence is perfect. This might not be the situation with the experimental data. As a result, the simulations could over-predict the lift force and hence the vibration amplitude.

The displacement phase plots for Sg = 0·01, 0·1, 1·0 and 10 are shown in Figure 6(a–d). These plots clearly show that the oscillations are self-limiting and they all appear to have a "figure of 8" shape. As Sg changes from 0·01 to 0·1, the amplitude of the vibration appears to remain the same. However, as Sg increases to 10.0, the amplitude decreases sharply; see Figure 6(d). Note that the equilibrium position of the vibration in the streamwise direction is not zero as the cylinder is subject to a mean drag force. This position changes as Sg varies.

Nonlinear vortex-induced vibrations. Flow-induced vibrations on an elastic structure are, in general, nonlinear. The vibration of the structure affects the fluid flow around the structure which, in turn, changes the induced forces on the structure and hence the structural response. In order to have a significant vortex-induced response, the frequency ratio f_n/f_s^* is chosen to vary from 0·65 to 5·2 with most of the cases concentrated around $f_n/f_s^* = 1$. The results of the mean drag coefficient $C_{d\,mean}$, the root-mean-square values of

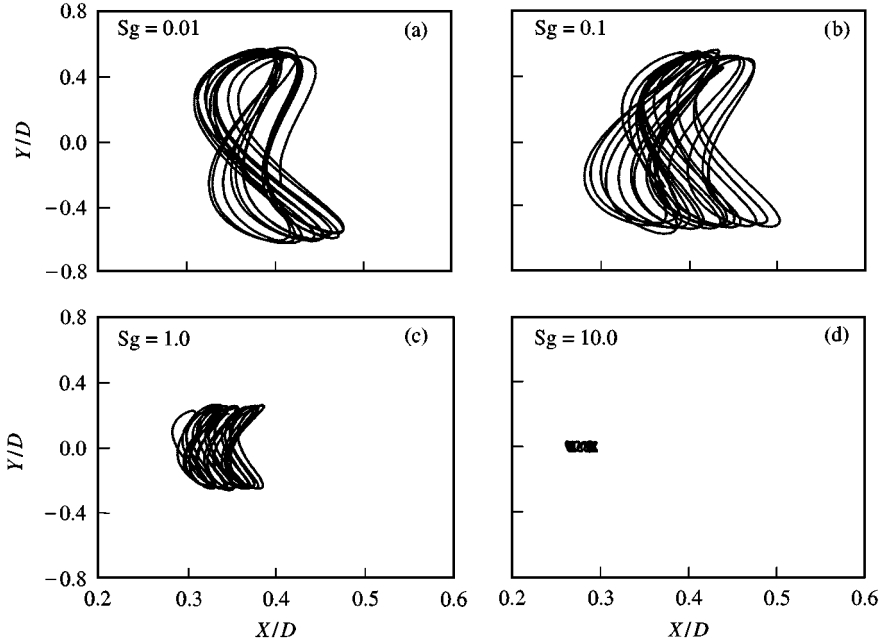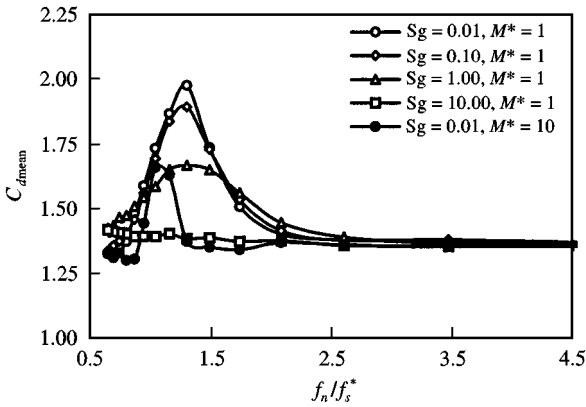Figure 6. X–Y phase plot for the case with $M^* = 1$ and $f_n/f_s^* = 1\cdot 30$.

Figure 7. Variation of the mean drag coefficient with f_n/f_s.

the cross-flow amplitude Y_{rms} of the cylinder and the lift coefficient C_{lrms} and the vortex-shedding frequency ratio f_s/f_s^*, versus the frequency ratio f_n/f_s^*, are shown in Figures 7, 8, 9 and 10, respectively.

It is seen that all the parameters behave similarly. That is, as the ratio f_n/f_s^* increases, the parameters increase, reach their respective maxima, then decrease and approach a constant value representative of that of the rigid cylinder. It is noted that both the amplitude of vibration of the cylinder and the drag coefficient reach their maximum values at the frequency ratio $f_n/f_s^* = 1\cdot 3$ for the mass ratio $M^* = 1$ (see Figures 7 and 8), where the maximum values for $C_{d\,mean}$ and $2Y_{rms}/D$ are $2\cdot 0$ and $0\cdot 8093$, respectively. It will be seen later that the vortex structure in the wake in this case undergoes dramatic changes compared
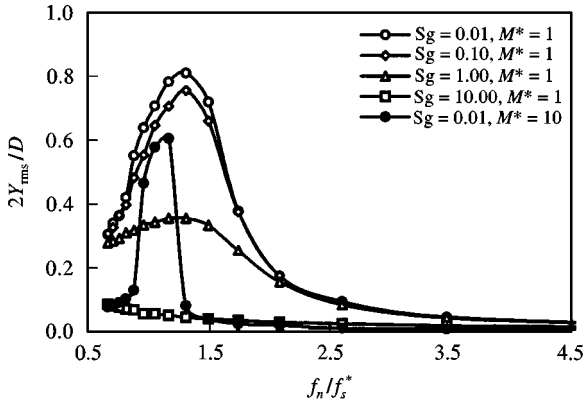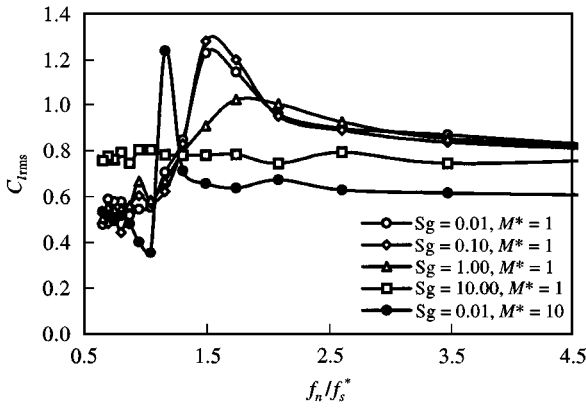
Figure 8. Variation of Y_{rms} with f_n/f_s^*.
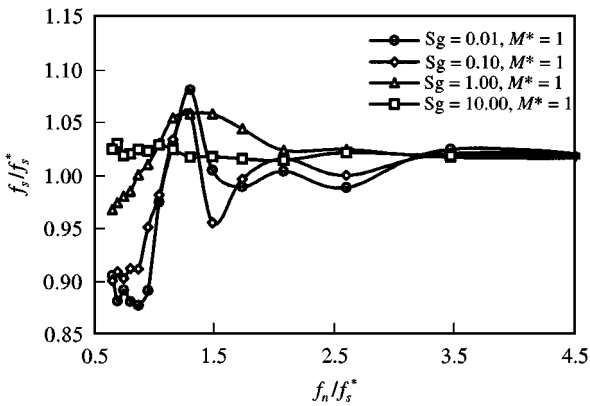
Figure 9. Variation of C_{lrms} with f_n/f_s^*.

Figure 10. Variation of the vortex-shedding frequency with f_n/f_s^*.

with the rigid cylinder case. For the $M^* = 10$ case, the maximum values for $C_{d\,mean}$ and $2Y_{rms}/D$ occur at $f_n/f_s^* = 1.04$ with corresponding maximum values given by 1.6587 and 0.6032, respectively. Generally, the most violent vibration is expected to happen when the vibration frequency of the cylinder is about the same as the natural frequency of the

fluid–structure system. The difference in the frequency ratio, where the peak values of $C_{d\,\mathrm{mean}}$ and $2Y_{\mathrm{rms}}/D$ occur for the $M^* = 1$ and $M^* = 10$ cases, indicates the effect of M^* on the natural frequency of the fluid–structure system.

In fact, if the right-hand side of (7) is re-written into a fluid force plus an inertia force (added mass) term, which depends on the acceleration of the cylinder, the effect of the added mass on the natural frequency of the fluid–structure system can be estimated. This, in turn, explains why the peak values occur at around 1·30 and 1·04 for the $M^* = 1$ and $M^* = 10$ case, respectively. If the added mass term in equation (7) is moved from the right-hand side to the left-hand side, the resulting equation can be re-arranged to give

$$\frac{d^2\chi}{dt^2} + 2\alpha^*\omega_n^* \frac{d\chi}{dt} + \omega_n^{*2}\chi = \frac{\mathbf{F}_1(t)}{m + (\pi/4)\rho D^2}, \tag{12}$$

where the induced force is $\mathbf{F}_1(t) = \mathbf{F}(t) + (\pi\rho D^2/4)(d^2\chi/dt^2)$, $\alpha^* = \alpha/\sqrt{1 + (\pi/4M^*)}$, and $\omega_n^* = \omega_n/\sqrt{1 + (\pi/4M^*)}$. The natural frequency of the fluid-structure system can then be deduced to be

$$f_n^* = \frac{f_n}{\sqrt{1 + (\pi/4M^*)}}. \tag{13}$$

For the $M^* = 1$ case, $\sqrt{1 + (\pi/4M^*)} = 1\cdot3362$; therefore, according to (13), $f_n^*/f_s^* = 0\cdot97$ when $f_n/f_s^* = 1\cdot30$, while for the $M^* = 10$ case, $\sqrt{1 + (\pi/4M^*)} = 1\cdot0385$, which gives $f_n^*/f_s^* \approx 1$ for $f_n/f_s^* = 1\cdot04$. This indicates that f_n^*, the natural frequency of the fluid–structure system, is in fact very close to the natural shedding frequency f_s^* in these two cases although the structural frequency f_n is not. Therefore, it is not surprising to see that the peak values of the vibration occurs at $f_n/f_s^* = 1\cdot30$ for the $M^* = 1$ case and at $f_n/f_s^* = 1\cdot04$ for the $M^* = 10$ case.

It can be seen that the peak bands of the $C_{d\,\mathrm{mean}}$, $2Y_{\mathrm{rms}}/D$ and $C_{l\,\mathrm{rms}}$ are much wider for the $M^* = 1$ case than for the $M^* = 10$ case. In other words, a lighter structure has a wider resonance band. The vibration amplitude of the cylinder obviously decreases as M^* increases, i.e., a heavier structure has less violent vibration. As f_n/f_s^* increases, the mean value of the drag coefficient approaches a constant value of 1·32, which is the value for the rigid cylinder, and the value of $2Y_{\mathrm{rms}}/D$ tends to zero. The value of $C_{l\,\mathrm{rms}}$ appears to be more scattered than other parameters. Even when f_n/f_s^* is about 4·5, $C_{l\,\mathrm{rms}}$ still shows a dependence on Sg.

The results further show that the peak-to-peak amplitude $2Y_{\mathrm{rms}}/D$ decreases as Sg increases. When Sg reaches 10, $2Y_{\mathrm{rms}}/D$ is as small as $0\cdot1D$, and $C_{d\,\mathrm{mean}}$ approaches 1·32. It is noted that the maximum value of $C_{l\,\mathrm{rms}}$ appears at a higher value of f_n/f_s^* than the corresponding maxima for $C_{d\,\mathrm{mean}}$ and Y_{rms}. This trend is also indicated in the results of Newman & Karniadakis (1997). For higher values of M^*, the peak of the $C_{l\,\mathrm{rms}}$ occurs at a lower value of f_n/f_s^*. Around the peaks of the $M^* = 1$ and $M^* = 10$ cases, the value of the $C_{l\,\mathrm{rms}}$ is greater than 1·2.

In Figure 10, it can be seen that for the higher reduced damping Sg = 10·0, the vortex shedding frequency is about the same as the natural vortex-shedding frequency for the rigid cylinder. While for lower values of Sg, such as Sg = 0·01, 0·1 or 1, the vortex-shedding frequency is lower than f_s^* when f_n/f_s^* is less than 1. As the natural frequency of the cylinder increases and switches over f_s^*, the vortex-shedding frequency f_s increases and reaches a maximum value around $f_n/f_s^* = 1\cdot30$ (for the $M^* = 1$ case), and gradually tends to f_s^*. This indicates that the vortices shed at a maximum frequency when the maximum vibration amplitude and the maximum drag coefficient have been reached. The vortex structure in the near wake at this frequency ratio is discussed in the following section.

6. THE $M^* = 1$ AND Sg $= 0·01$ CASE

In order to further understand the results presented in the previous sections, the force and the displacement time histories and the wake structure of the $M^* = 1$ and Sg $= 0·01$ case are examined in detail.

6.1. VORTEX STRUCTURE IN THE WAKE

Figure 11 shows the comparison of the vortex pattern in the wake of the elastic cylinder at different frequency ratios. When the natural frequency of the cylinder is far from the vortex shedding frequency, for example $f_n/f_s^* = 5·2$ and $2·6$ [Figures 11(a) and 11(b)], the vortex pattern is very similar to the one shown for the rigid cylinder (Figure 3). As the frequency ratio decreases, the cylinder vibration starts to affect the vortex pattern in the wake. The separation distances between vortices in the transverse and streamwise directions and the width of the vortex wake start to change. When $f_n/f_s^* = 1·49$ [Figure 11(d)], the vortex spacing in the near wake in both the transverse and streamwise directions become much smaller. Two batches of the vortices are seen in Figure 11(d). It seems that the vortex shedding at one frequency is broken up by another frequency. This is obviously seen from the force time-histories to be presented later for this case. When the
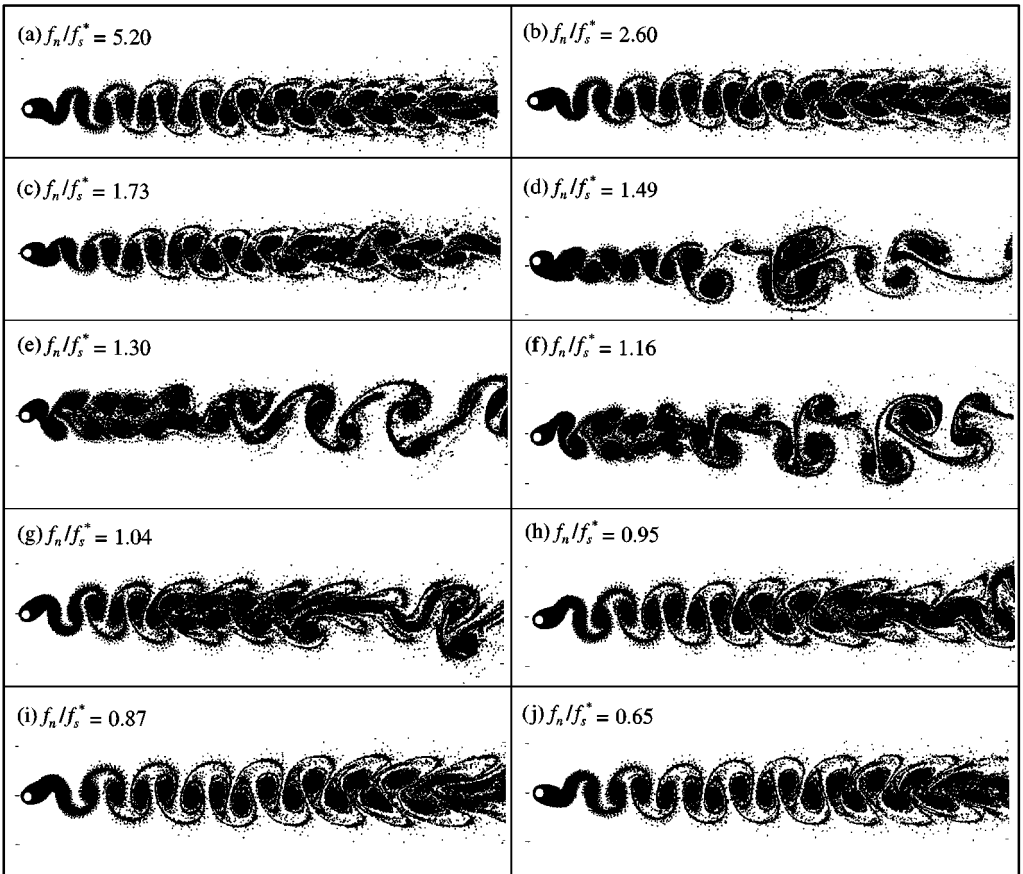

(a) $f_n/f_s^* = 5.20$

(b) $f_n/f_s^* = 2.60$

(c) $f_n/f_s^* = 1.73$

(d) $f_n/f_s^* = 1.49$

(e) $f_n/f_s^* = 1.30$

(f) $f_n/f_s^* = 1.16$

(g) $f_n/f_s^* = 1.04$

(h) $f_n/f_s^* = 0.95$

(i) $f_n/f_s^* = 0.87$

(j) $f_n/f_s^* = 0.65$

Figure 11. Vortex pattern in the wake of an elastic cylinder for the case Sg $= 0·01$ and $M^* = 1$.

frequency ratio is near 1·30, the vortices shed from the cylinder form two parallel rows with opposite sign of the vortices in the near wake [Figure 11(e)]. The vortex spacings appear to become even smaller in the streamwise direction and wider in the transverse direction. These spacing changes between the vortices are due to the fact that the vortices are shed at a higher frequency in these cases (Figure 10), thus leading to a narrowing of the streamwise distance of the vortices. It is further noticed that, in both the $f_n/f_s^* = 1·49$ and $f_n/f_s^* = 1·30$ cases, the cylinder vibrates with a rather large amplitude (Figure 8). However, the width of the near wake for the $f_n/f_s^* = 1·30$ case is much wider than that for the $f_n/f_s^* = 1·49$ case [see Figure 11(d, e)]. It could be due to the fact that the vortex is shed at a different position relative to the cylinder. For the former case ($f_n/f_s^* = 1·30$), the vortex sheds at the end of each vibration cycle, which increases the lateral spacing of the vortices, while for the latter case, the vortex sheds at the middle of the vibration cycle.
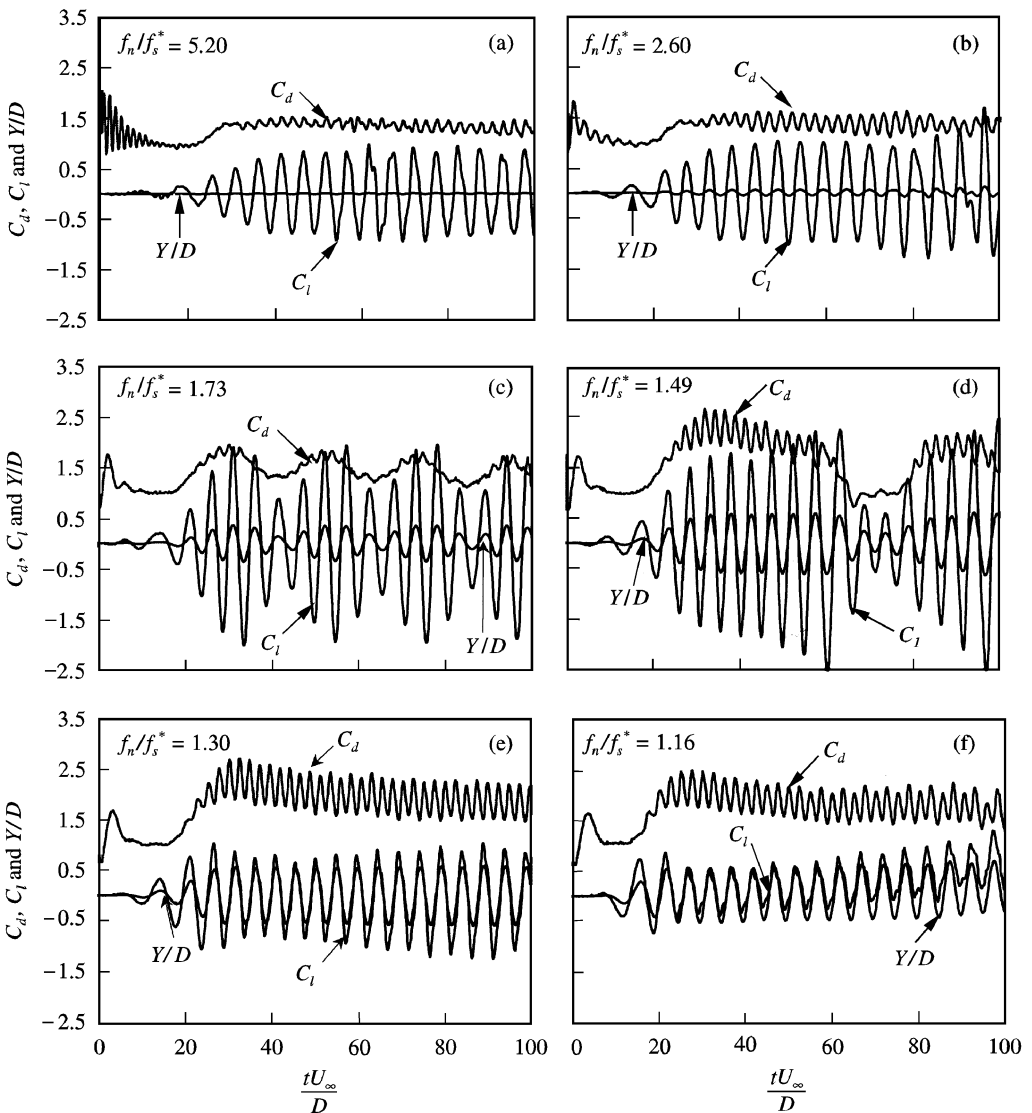

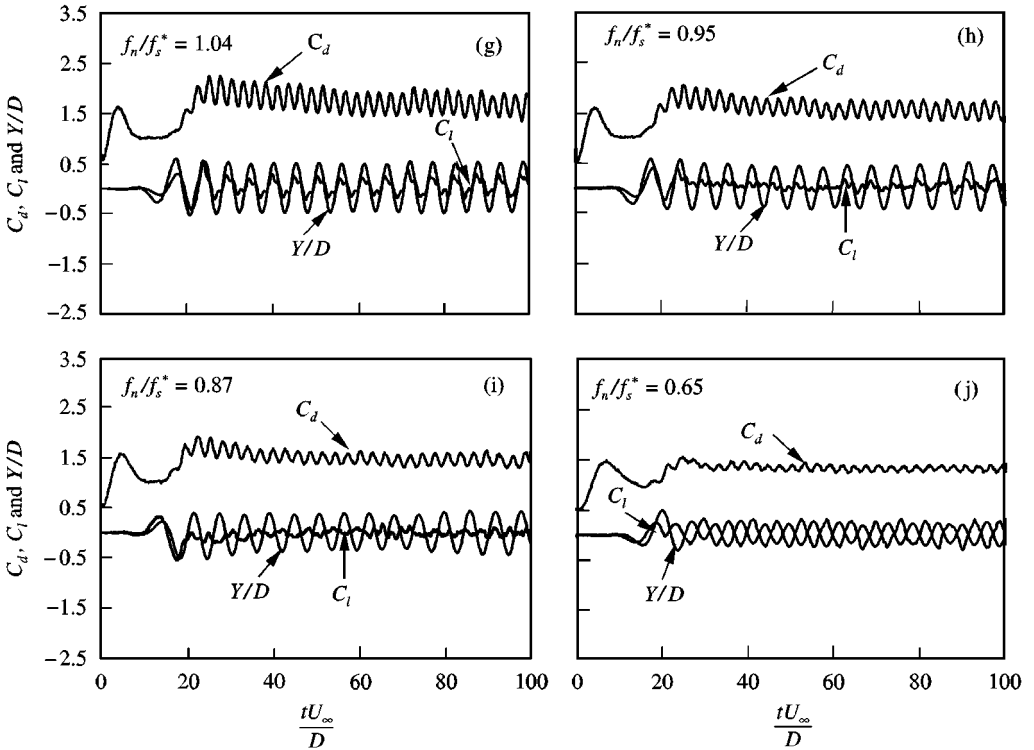Figure 12. Force and displacement time-histories for the case Sg = 0·01 and $M^* = 1$.

Figure 12. Force and displacement time-histories (continued).

The two parallel vortex rows in the $f_n/f_s^* = 1.30$ case do not persist for a long distance due to their instability. It is obvious that the ratio of the lateral to streamwise vortex spacing is much larger than the limit for the stable Karman vortex street (see Figure 3). Therefore, the wake starts at a distance about $20D$ from the cylinder in this case to reorganise itself and tries to form a Karman-vortex-street-like pattern with a lower frequency [Figure 11(e)]. A similar phenomenon is also observed in the $f_n/f_s^* = 1.16$ case, but a "P + S" pattern (Williamson & Roshko 1988) rather than the Karmen-vortex-street-like vortex is seen after the two parallel vortex rows lose their stability. As the frequency ratio f_n/f_s^* decreases further to 0.87 and 0.65, the vortex shedding frequency ratio f_n/f_s^* decreases and this expands the streamwise vortex spacing as shown in Figures 11(i, j).

The vibration of the cylinder generally enlarges the width of the wake and strengthens the vortices shed from the cylinder. As a result, the mean value of the drag coefficient increases and reaches a maximum when the cylinder reaches its maximum vibration amplitude as shown in Figures 7 and 8.

6.2. FORCE TIME HISTORY AND CROSS-FLOW RESPONSE

Figure 12 shows the time histories of the drag and lift force together with the cross-flow displacement Y of the cylinder. It should be noted that, at high values of f_n/f_s^*, these time histories are very similar to those shown for a rigid cylinder [cf. Figure 3 with Figures 12(a, b)]. At lower values of f_n/f_s^*, several interesting features can be observed.

Firstly, in Figure 12(c), the lift force and the cross-flow displacement of the cylinder show a beating behaviour when $f_n/f_s^* = 1.73$. The drag force distinctly shows two major

frequencies, while the vortex pattern in the wake [Figure 11(c)] also starts to deviate from the rigid cylinder pattern [Figures 11(a, b)]. The changes are quite obvious when the frequency ratio f_n/f_s^* decreases to 1·49 [Figure 11(d)]. In this case, the vortex shedding frequency is interrupted by a lower frequency [Figure 12(d)]. It is obvious that, in order to get more accurate results for this case, the calculations need to be carried out for a longer period of time.

Secondly, the mean drag increases when the amplitude of the vibrations increases (Figure 12(e–f)). It is further noticed that the amplitude of the oscillating part of the drag force also increases. This is most evident when the amplitude reaches its maximum value [Figure 12(e)]. The amplitude of the drag force is as large as one-third of the amplitude of the lift force. However, the results show that the oscillation in the streamwise direction is still one order smaller than that in the transverse direction.

Thirdly, the phase between lift force and the cross-flow displacement undergoes an interesting change from the 'in-phase' to the 'out-of-phase' mode as the freuqency ratio f_n/f_s^* varies from greater than 1 to smaller than 1 [Figure 12(g, h)]. The switch seems to occur when $f_n/f_s^* \sim 0.95$ [Figure 12(h)]. The amplitude of the lift force appears to reach its minimum value at this frequency ratio. Higher harmonics are present in the lift time history. Interestingly, the response of the cylinder appears to be very regular. When $f_n/f_s^* < 0.87$, the lift force and the displacement is completely "out-of-phase" [Figure 12(i, j)].

7. COMPARISON OF THE ONE- AND TWO-DEGREE-OF-FREEDOM CASES

Finally, a one-degree-of-freedom case with Sg = 0·01 and, $M^* = 1$, where the cylinder is only allowed to vibrate in the transverse direction, is calculated and the results are compared with those for the two-degree-of-freedom case. The comparisons for the mean drag, the unsteady lift, the displacement in the transverse direction, and the vortex shedding frequency are shown in Figures 13, 14, 15, and 16, respectively. In these figures, the open circles represent the results of the two-degree-of-freedom case.

It is seen that the mean drag force for the two cases are essentially equal. The peak-to-peak amplitude $2Y_{rms}/D$ appears to have a higher value for the two-degree-of-freedom case than for the one-degree-of-freedom case, especially around the frequency range $f_n/f_s^* = 1.0$ to 1·5, while the peak value occurs at a different value of f_n/f_s^*. The $C_{l rms}$ also shows a very similar behaviour. However, the comparison of f_s shows that the vortex-shedding frequency
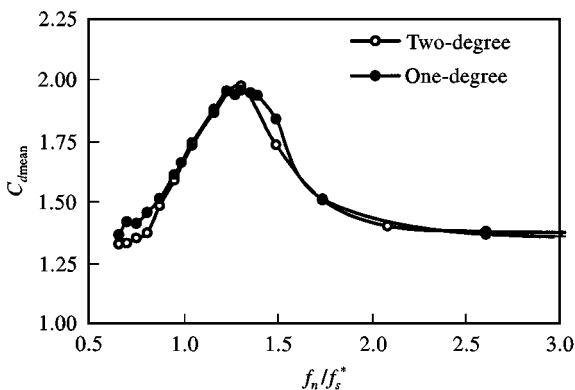

Figure 13. Comparison of $C_{d\,mean}$ for the Sg = 0·01 and $M^* = 1$ case.

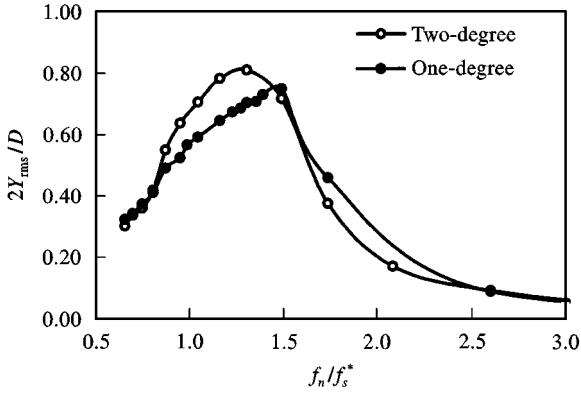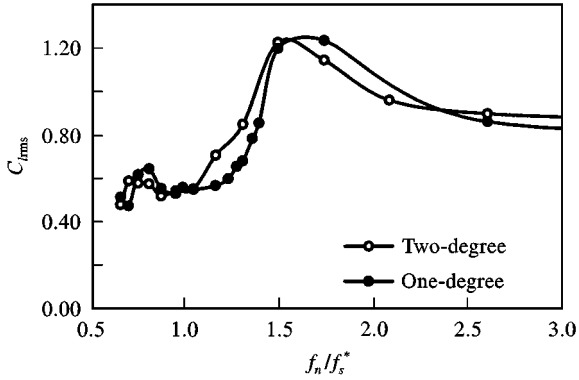Figure 14. Comparison of Y_{rms}/D for the $Sg = 0.01$ and $M^* = 1$ case.

Figure 15. Comparison of C_{lrms} for the $Sg = 0.01$ and $M^* = 1$ case.
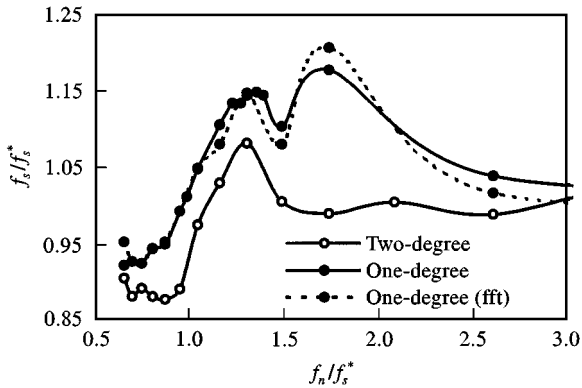

Figure 16. Comparison of f_s/f_s^* for the $Sg = 0.01$ and $M^* = 1$ case.

for the one-degree-of-freedom case has a similar trend but is generally higher than that shown for the two-degree-of-freedom case. The shedding frequency is evaluated from the lift force time histories using the ARMA and FFT techniques.
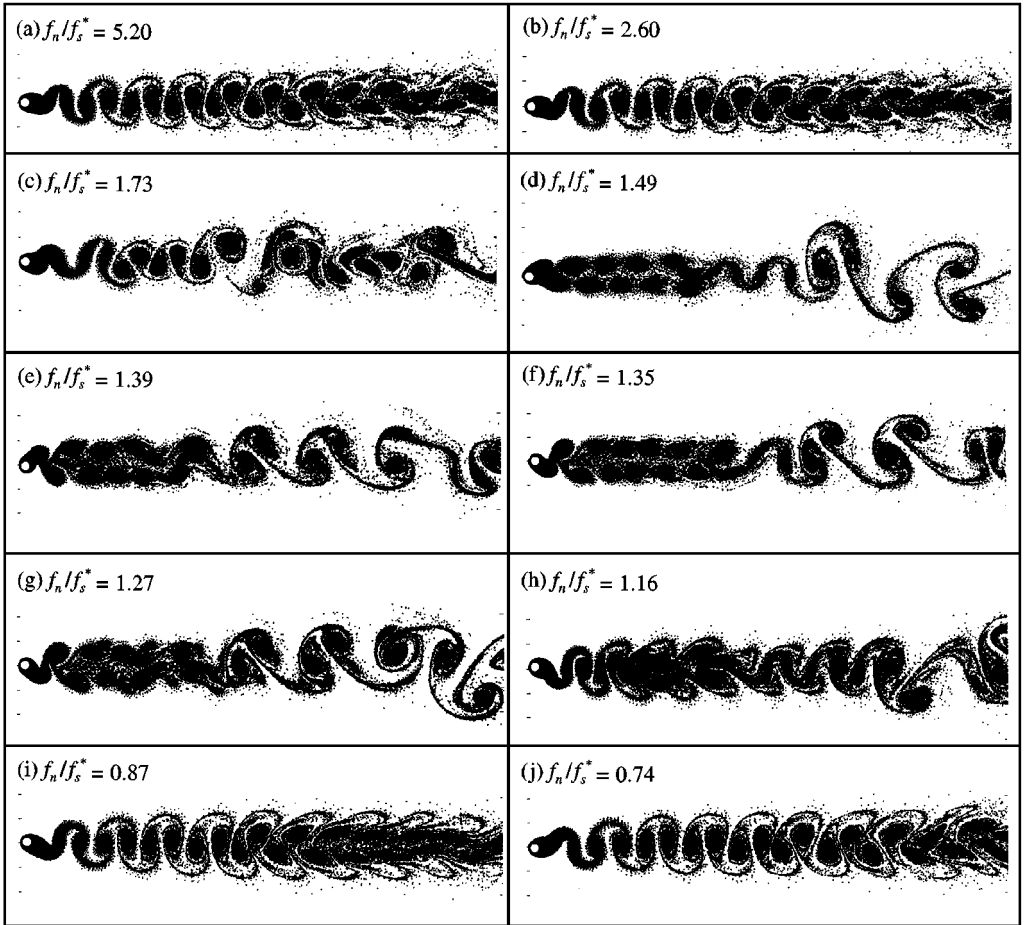
Figure 17. Vortex pattern in the wake of an elastic cylinder with a one-degree-of-freedom motion for the Sg $= 0.01$ and $M^* = 1$ case.

Figure 17 shows the vortex pattern for the one-degree-of-freedom case. Compared with the vortex pattern shown in Figure 11 for the two-degree-of-freedom case, it can be seen that the two cases experience similar changes in the wake vortex patterns as the frequency ratio f_n/f_s^* varies from 5·2 to 0·65. However, it is found that the values of f_n/f_s^* in which the calculated wake displays similar vortex pattern change are higher for the one-degree-of-freedom case than for the two-degree-of-freedom case. In other words, similar vortex patterns always come up late in the two-degree-of-freedom case as the value of f_n/f_s^* varies from 5·2 to 0·65. This is why the peak value of Y_{rms} occurs at a higher value of f_n/f_s^* for the one-degree-of-freedom case compared to that given by the two-degree-of-freedom case (Figure 14).

Figure 18 shows the force and displacement time-histories for the one-degree-of-freedom case. It should be pointed out that the amplitude of the drag force is larger than that shown in the two-degree-of-freedom case. For $f_n/f_s^* = 1·30$, the amplitude of the drag force oscillation is even larger than that of the lift force, which is not observed in the two-degree-of-freedom case. It is found that the phase switch from the 'in-phase' to the 'out-of-phase' occurs at $f_n/f_s^* \sim 1·04$, which is higher than the corresponding value for the two-degree-of-freedom case.
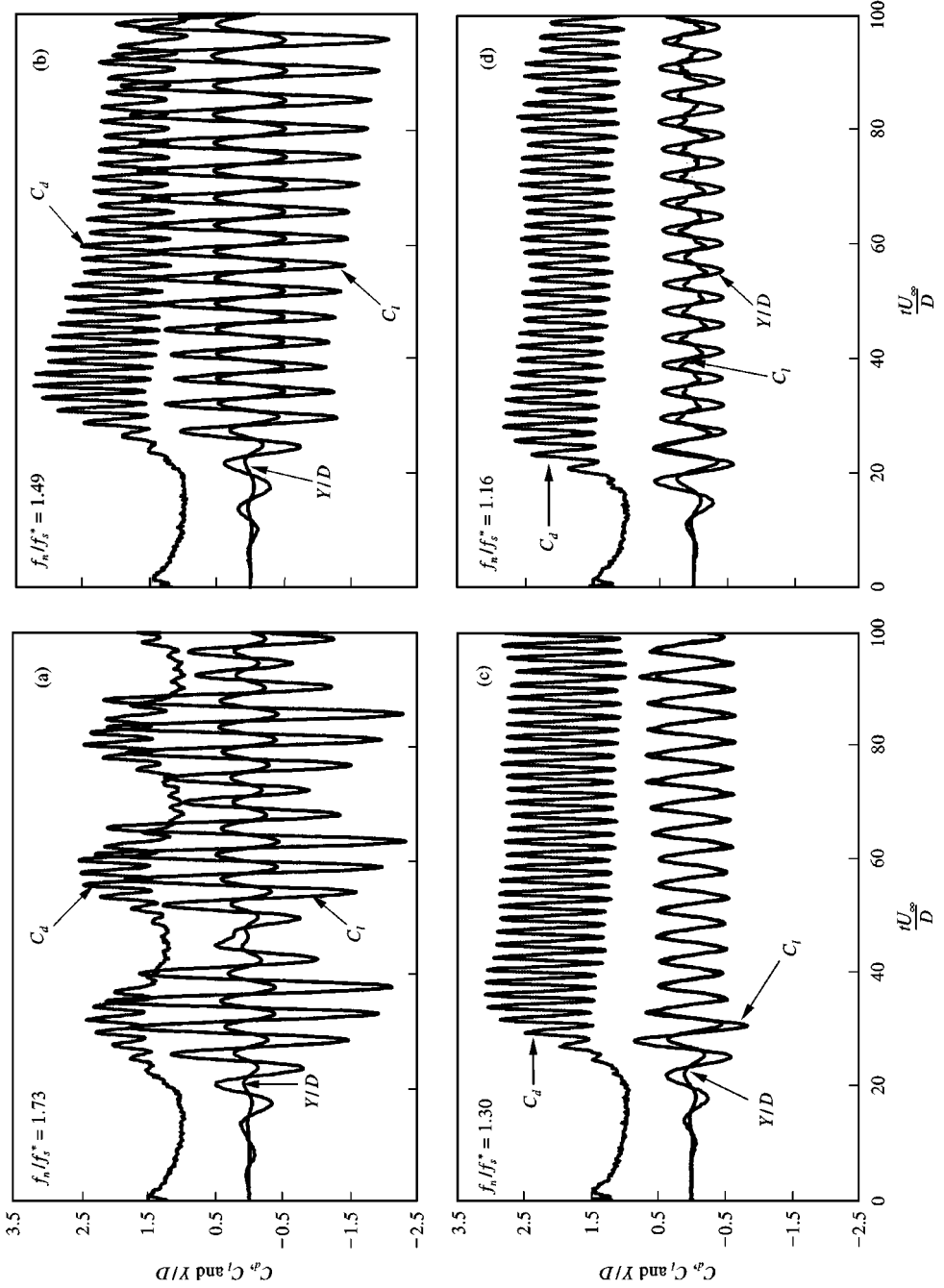
Figure 18. Time-histories of C_d, C_l and Y/D for the one-degree-of-freedom case with $Sg = 0.01$ and $M^* = 1$.
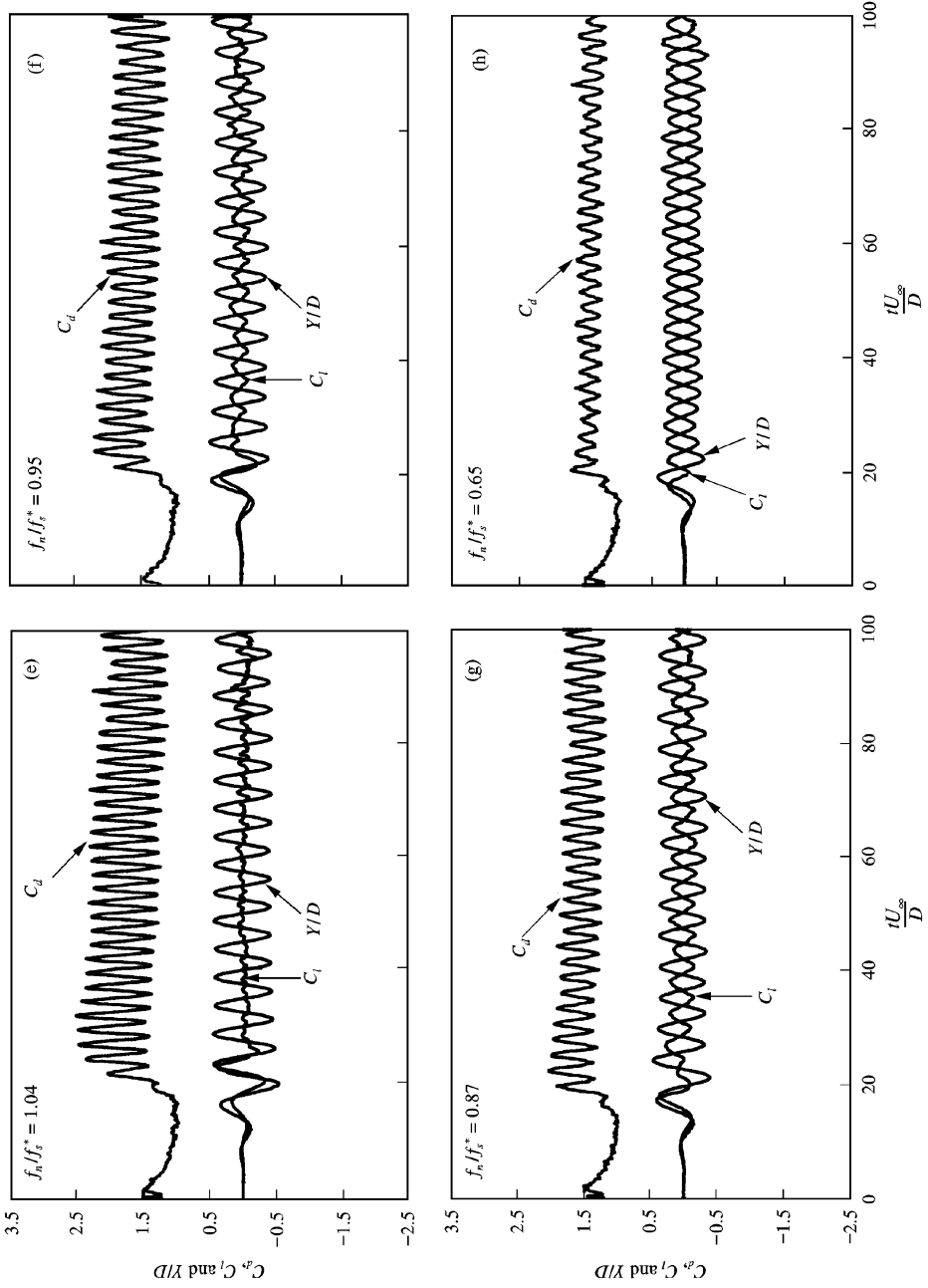
Figure 18. Time-histories of C_d, C_l and Y/D (continued).

8. CONCLUSIONS

This paper presents a numerical study of a uniform flow past an elastic circular cylinder using the VIC discrete vortex method. The Reynolds number is kept at 200 for all calculations. The cylinder motion is modelled by a spring–damper–mass system. Two groups of calculations have been carried out. In the first group, the cylinder is allowed to vibrate only in the transverse direction (one degree of freedom), while in the second, the cylinder is free to vibrate in both the transverse and streamwise directions. The response of the cylinder, the induced forces, the vortex-shedding frequency and the vortex structure in the wake are examined in detail. This study, therefore, complements that of Slaouti & Stansby (1994) and examines the interaction behaviour in greater detail than before.

The calculated results are compared with previous experimental and computational data. The amplitude of the limit-cycle oscillations is in reasonable agreement with previous results. The present results further show that the vortex-induced vibration can be quite violent. The amplitude of the transverse vibration can be as high as $0.57D$ for the cases covered in this investigation. The mean drag force also increases substantially. When the vibration amplitude of the cylinder reaches its maximum value, the vortex pattern in the wake undergoes significant changes, thus leading to a substantial alteration of the vortex spacings.

It is shown that the vibration level not only depends strongly on the reduced damping parameter, Sg, but is also affected by the mass ratio, M^*. The mass ratio has a strong influence on the natural frequency of the fluid-structure system. To quantitatively estimate the influence, further study is needed.

The results from the two groups are compared. The comparison shows that the behaviour of the quantities in the transverse direction for the two cases are quite similar qualitatively but there are some quantitative differences. This suggests that the streamwise motion of the body does influence the motion in the transverse direction, even though the transverse motion is dominant for a bluff body in a cross-flow. In other words, a one-degree-of-freedom structural model might not be sufficient in the analysis of vortex-induced vibrations of a circular cylinder in a cross-flow.

Although the present two-dimensional approach cannot capture the three-dimensional effects in the wake, the technique can still be used to extract meaningful physics and the salient features of vortex-induced vibrations on a bluff body.

REFERENCES

ARKELL, R. H., GRAHAM, J. M. R. & ZHOU, C. Y. 1992 The effects of waves and mean flow on the hydrodynamic forces on circular cylinders. *Proceedings of the 6th BOSS Conference*, London, 1992, 445–451.

BABAN, F., SO, R. M. C. & OTUGEN, M. V. 1989 Unsteady forces on circular cylinders in a cross-flow. *Experiments in Fluids* **7**, 293–302.

BEARMAN, P. W. 1984 Vortex shedding from oscillating bluff bodies. *Annual Review of Fluid Mechanics* **16**, 195–222.

BENDAT, J. S. & PIERSOL, A. G. 1971 *Random Data*: *Analysis and Measurement Procedures*. Wiley-Interscience, NJ.

BLEVINS, R. D. 1994 *Flow-Induced Vibration.* Malabar, FL Krieger Publishing Company.

BRIKA, D. & LANEVILLE, A. 1993 Vortex-induced vibrations of a long flexible circular cylinder. *Journal of Fluid Mechanics* **250,** 481–508.

CARRIER, J., GREENGARD, L. & ROKHLIN, V. 1988 A fast adaptive multipole algorithm for particle simulations. *SIAM Journal of Science and Statistical Computing* **9,** 669–686.

CHORIN, A. J., 1973 Numerical study of slightly viscous flow. *Journal of Fluid Mechanics* **57,** 785–796.

CHASTIANSEN, J. P. 1973 Numerical simulation of hydrodynamics by the method of point vortices. *Journal of Computational Physics* **13,** 363–379.

DOWNIE, M. J., GRAHAM, J. M. R., ZHAO, Y. D. & ZHOU, C. Y. 1995 Effects of transverse vibration on the hydrodynamic damping of an oscillating bluff body. In *Flow-Induced Vibration* ed. P. W. Bearman, pp. 193–203. Rotterdam: Balkema.

FEIREISEN, J. M., MONTGOMERY, M. D. & FLEETER, S. 1994 Unsteady aerodynamic forcing functions: a comparison between linear theory and experiment. *Journal of Turbomachinery* **116,** 676–685.

FENG, C. C. 1968 The measurement of vortex-induced effects in flow past stationary and oscillating circular and d-section cylinders. M.A.Sc. thesis, University of British Columbia, Vancouver, B. C., Canada.

GRAHAM, J. M. R. 1988 Computation of viscous separated flow using a particle method. In *Numerical Methods in Fluid Mechanics* (ed. K. W. Morton). Vol. 3, pp. 310–317. Oxford: Oxford University Press.

GRAHAM, J. M. R., ARKELL, R. H. & ZHOU, C. Y. 1993 The effect of combinations of mean current and oscillatory flow on the forces induced on a bluff body. *Journal of Wind Engineering and Industrial Aerodynamics* **50,** 85–96.

GRIFFIN, O. M. & VOTAW, C. W. 1972 The vortex street in the wake of a vibrating cylinder. *Journal of Fluid Mechanics* **51,** 31–48.

GRIFFIN, O. M. & RAMBERG, S. 1974 The vortex-street wakes of vibrating cylinders. *Journal of Fluid Mechanics* **66,** 553–576.

GRIFFIN, O. M. & KOOPMANN, G. H. 1977 The vortex-excited lift and reaction forces on resonantly vibrating cylinders. *Journal of Sound and Vibration* **54,** 435–448.

GRIFFIN, O. M. 1980 Vortex-excited cross-flow vibrations of a single cylindrical tube. *ASME Journal of Pressure Vessel Technology* **102,** 158–166.

GRIFFIN, O. M. & RAMBERG, S. E. 1982 Some recent studies of vortex shedding with application to marine tubulars and risers. *ASME Journal of Energy Resources Technology* **104,** 2–13.

GRIFFIN, O. M. 1992 Vortex-induced vibrations of marine structures in uniform and sheared currents. NSF Workshop on Riser Dynamics, University of Michigan.

HALL, K. C. 1994 Eigenanalysis of unsteady flows about airfoils, cascades, and wings. *AIAA Journal* **32,** 2426–2432.

JADIC, I., SO, R. M. C. & MIGNOLET, M. P. 1998 Analysis of fluid-structure interactions using a time marching technique. *Journal of Fluids and Structures* **12,** 631–654.

KHALAK, A. & WILLIAMSON, C. H. K. 1996 Dynamics of a hydro-elastic cylinder with very low mass and damping. *Journal of Fluids and Structures* **10,** 455–472.

KOOPMANN, G. H. 1967 The vortex wakes of vibrating cylinders at low Reynolds numbers. *Journal of Fluid Mechanics* **28,** No. 3, 501–512.

MENEGHINI, J. R. & BEARMAN, P. W. 1993 Numerical simulation of high amplitude oscillatory-flow about a circular cylinder using a discrete vortex method. *Proceedings of AIAA Shear Flow Conference*, Paper No. AIAA 93-3288, Orlando, FL, July 6–9, 1993.

MIGNOLET, M. P. RED-HORSE, J. R. & LIN, C. C. 1993 A multistage ARMAX identification of structures. *Proceedings of the AIAA/ASME 34th Structures, Structural Dynamics, and Materials Conference*, La Jolla, CA, 19–22 April, pp. 3366–3374.

MIGNOLET, M. P. & RED-HORSE, J. R. 1994 ARMAX identification of vibrating structures: model and model order estimation. *Proceedings of the AIAA/ASME 35th Structures, Structural Dynamics, and Materials Conference.* Hilton Head, SC, 18–20 April, pp. 1628–1637.

NEWMAN, D. J. & KARNIADAKIS, G. E. 1995 Direct numerical simulations of flow over a flexible cable. In *Flow-Induced Vibration* (ed. P. W. Bearman). pp. 193–203. Rotterdam: Balkema.

NEWMANN, D. J. & KARNIADAKIS, G. E. 1997 A direct numerical simulation study of flow past a freely vibrating cable. *Journal of Fluid Mechanics*, **344,** 95–136.

PARKINSON, G. 1989 Phenomena and modelling of flow-induced vibrations of bluff bodies. *Progress in Aerospace Science* **26,** 169–224.

RICHTER, A. & NAUDASCHER, E. 1976 Fluctuating forces on a rigid circular cylinder in confined flow. *Journal of Fluid Mechanics* **78,** 561–576.

SARPKAYA, T. 1979 Vortex-induced oscillations. *Journal of Applied Mechanics* **46,** 241–258.

SLAOUTI, A. & STANSBY, P. K. 1992 Flow around two circular cylinders by the random-vortex method. *Journal of Fluids and Structures* **6,** 641–670.

SLAOUTI, A. & STANSBY, P. K. 1994 Forced oscillation and dynamics response of a cylinder in a current investigation by the vortex method, *Proceedings BOSS '94 Conference MIT*, pp. 645–654.

SO, R. M. C. & SAVKAR, S. D. 1981 Buffeting forces on rigid circular cylinders in cross flows. *Journal of Fluid Mechanics* **105,** 397–425.

SO, R. M. C., JADIC, I. & MIGNOLET, M. P. 1998 Fluid-structure resonance produced by oncoming alternating vortices. *Journal of Fluids and Structures*, submitted.

STANSBY, P. K. & SMITH, P. A. 1983 Simulation of flows around cylinders by a Lagrangian vortex scheme. *Applied Ocean Research* **5,** 167–178.

STANSBY, P. K. & SMITH, P. A. 1991 Viscous forces on a circular cylinder in orbital flow at low Keulegan-Carpenter numbers. *Journal of Fluid Mechanics* **229,** 159–171.

STANSBY, P. K. & SLAOUTI, A. 1993 Simulation of vortex shedding including blockage by the random-vortex and other methods. *International Journal for Numerical Methods in Fluids* **17,** 1003–1013.

WEST, G. S. & APELT, C. J. 1997 Fluctuating lift and drag forces on finite lengths of a circular cylinder in the subcritical Reynolds number range. *Journal of Fluids and Structures* **11,** 135–158.

WILLIAMSON, C. H. K. & ROSHKO, A. 1988 Vortex formation in the wake of an oscillating cylinder. *Journal of Fluids and Structures* **2,** 355–381.

WILLIAMSON, C. H. K. 1989 Oblique and parallel models of vortex shedding in the wake of a circular cylinder at low Reynolds numbers. *Journal of Fluid Mechanics* **206,** 579–627.

WILLIAMSON, C. H. K. 1991 2-D and 3-D aspects of the wake of a cylinder, and their relation to wake computations. *Lectures of Applied Mathematics*, Vol. 28, pp. 719–751. Providence, RI: American Mathematical Society.

ZHOU, C. Y. 1994 Effects of combination motion on cylinders in waves and currents. Ph.D. thesis, Imperial College, University of London, U.K.